Dihexadecyl Phosphate Monolayer Supported $[Ru(bpy)_3]^{2+}$ Crystallites Investigated by Near-Field Scanning Optical Microscopy

Frédéric Guérin, Yongchi Tian, and Janos H. Fendler*

Center for Advanced Materials Processing and Department of Chemistry, Clarkson University, Potsdam, New York 13699-5814

Received: February 25, 1999

Surface pressure (Π) vs surface area (*A*) isotherms of dihexadecyl phosphate (DHP) monolayers floating on aqueous tris(2,2′-bipyridyl)ruthenium(II) chloride ($[Ru(bpy)_3][Cl_2]$) solutions have established the formation of liquid expanded (LE), liquid condensed (LC), and solid condensed (SC) phases. Repeated compression and expansion cycles lead to the irreversible formation of a SC phase. Horizontal lifting of a hydrophilic substrate through the monolayer resulted in the transfer of a layer of DHP-coated $[Ru(bpy)_3]^{2+}$ microcrystallites. Additional layers of DHP/$[Ru(bpy)_3]^{2+}$ micocrystallites have been transferred by Schaefer's method. The presence of $[Ru(bpy)_3]^{2+}$ microcrystallites in the transferred multilayers has been established by absorption and fluorescence spectroscopies. The absorption and emission spectra of $[Ru(bpy)_3]^{2+}$ microcrystallites, grown under the DHP monolayers, had their maxima red-shifted and blue-shifted with respect to those observed for $[Ru(bpy)_3][Cl_2]$ in aqueous solution. Near-field scanning optical microscopy (NSOM) has been employed to spatially and spectrally resolve, at a submicron resolution, the presence of isolated seed crystals and their growth into differently shaped $[Ru(bpy)_3]^{2+}$ microcrystallites. NSOM also provided information on domain boundaries and on the partitioning of the fluorescent species into the various phases in the monolayer. Site-resolved near-field fluorescence spectroscopy provided evidence for the presence of $[Ru(bpy)_3]^{2+}$ microcrystallites in the circular domains formed under a DHP monolayer.

Introduction

Monomolecular layers of surfactants floating on aqueous solutions in a Langmuir trough have been shown to provide templates for the in situ generation of metallic, semiconducting, and magnetic nanoparticles and nanoparticulate films.[1] They have also been used to mediate the interfacial formation of a variety of inorganic and organic crystals from their supersaturated aqueous solutions[2,3] and to affect the aggregation behavior of cyanine dyes.[4−8] Electrostatic forces between the oppositely charged surfactant headgroups (carboxylate or phosphate ions, for example) and the precursor ions present in the aqueous subphase (calcium or sodium ions, for example) have been providing the primary driving force for strong interactions. Molecular complementary and lattice matching have often resulted in oriented crystallization.[2] Crystallization has also been investigated between the polar layers in Langmuir−Blodgett films containing metal ion complexes.[9−12]

The morphology of nanoparticles or nanocrystallites is expected to depend on the packing density and the phase of the monolayer under which they are formed. The present work has been designed to examine this dependency. We have investigated surface pressure (Π) vs surface area (*A*) isotherms of dihexadecyl phosphate (DHP) monolayers floating on aqueous tris(2,2′-bipyridyl)ruthenium(II) cations, $[Ru(bpy)_3]^{2+}$, and the optical spectroscopy and morphology of the structures formed on transferring these monolayers, along with the crystallites formed under them, onto solid substrates. Available information on DHP monolayers and $[Ru(bpy)_3]^{2+}$ dictated our choice.[9−12]

Advantage has been taken of the submicron spatial and spectral resolution power of near-field scanning optical microscopy (NSOM) to obtain simultaneously topographic and fluorescence images and near-field optical spectra of $[Ru(bpy)_3]^{2+}$ microcrystallites grown under DHP monolayers. In NSOM, light transmitted through a submicron aperture (<200 nm) in an opaque screen is used to form a spot, which is then scanned over an object and then collected to generate an image. If the aperture is in close proximity to the object to be resolved, i.e., within the near field (∼5−10 nm), then resolution is determined primarily by the size of the aperture rather than λ, the wavelength of the light, breaking the diffraction limit ($\lambda/2$) of the conventional optics.[15,18] Indeed, NSOM has been increasingly used for the characterization of nanodomains and even single molecules.[13−21] In the present work, simultaneous shear-force and high-resolution near-field optical imaging and spectroscopy have been used to provide valuable insight into the crystallization of cationic ruthenium complexes under anionic DHP monolayers as functions of the surface pressure and the conditioning of the monolayer.

Experimental Section

Materials. Dihexadecyl phosphate (DHP, Aldrich, 99%) in the acidic form and tris(2,2′-bipyridyl)ruthenium(II) chloride hexahydrate ($[Ru(bpy)_3][Cl_2]\cdot 6H_2O$, SIGMA) were used as received. Ultrapure water (pH 5.6 and resistivity 18 MΩ cm^{-1}) from a Millipore Milli-Q columns system provided with a Millipak filter (0.22 μm pore size) at the outlet was used for the subphase preparation.

Langmuir Monolayer Preparation. Langmuir monolayers were prepared by evenly spreading a calculated amount of chloroform ($CHCl_3$, Fisher, high-purity HPLC grade) solution of DHP (5.0×10^{-4} M) on pure water or on a 1.0×10^{-4} M aqueous solution of tris(2,2′-bipyridyl)ruthenium chloride in a

10.1021/jp990687d CCC: $18.00
Published on Web 08/31/1999

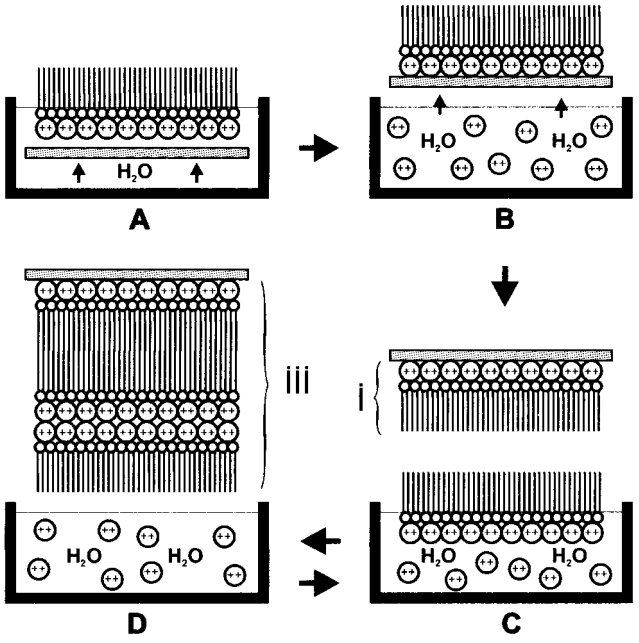

Figure 1. Schematics illustrating the transfer of a DHP monolayer, along with the $[Ru(bpy)_3]^{2+}$ crystallites grown under it (indicated by the larger circles containing ++), onto a solid substrate (steps A and B) for NSOM imaging and that for the transfer of additional DHP/$[Ru(bpy)_3]^{2+}$ layers by the Schaefer method (steps C, D repeated the required number of times; see Experimental Section for details).

commercial Lauda Model P film balance at ambient temperature (21 ± 2 °C). Prior to spreading the DHP, the surface of the subphase was cleaned by repeated compression, aspiration, and expansion cycles. The surface was deemed clean when the surface pressure increase was less than 0.2 mN/m upon compression to 20th of the original area and when this surface pressure increase remained the same after aging for 1 h. After allowing the solvent to evaporate for 15 min, the spread monolayer was then compressed at a constant barrier speed of 5 $Å^2$ mol^{-1} min^{-1}, and surface pressure (Π) vs surface area (*A*) isotherms of DHP monolayers were recorded simultaneously.

Transfer of DHP Monolayer Supported $[Ru(bpy)_3]^{2+}$ Crystallites onto Solid Substrates. Well-cleaned 0.15 mm thick microscope cover glasses (VWR Scientific for NSOM) or 1.0 mm thick quartz slides (for absorption and fluorescence spectroscopy) were used as substrates. The recommended procedure for cleaning glass substrates prior to deposition was followed. It involved the sonication (Branson 2200) of the glass slide in a solution of ionic detergent (Fisher Sparkleen1) for 20 min, thorough rinsing in deionized distilled water, exposure to pure ethanol vapors for 20 min, and finally drying in a stream of dry nitrogen.

Two different methods of transfer have been employed. The first method involved the introduction of the substrate into the subphase parallel to the water surface prior to the spreading of DHP. After monolayer formation the substrate was carefully lifted horizontally through the monolayer at a desired compression and/or after an appropriate conditioning by a mechanical lifting device. Identical protocol was used in the second method with the exception that the substrate was immersed into the subphase after the monolayer formation. Both methods resulted in the transfer of ruthenium complex crystallites onto the substrates with a DHP monolayer on their top such that the hydrocarbon tails of the surfactant remained exposed to air (steps A and B in Figure 1).

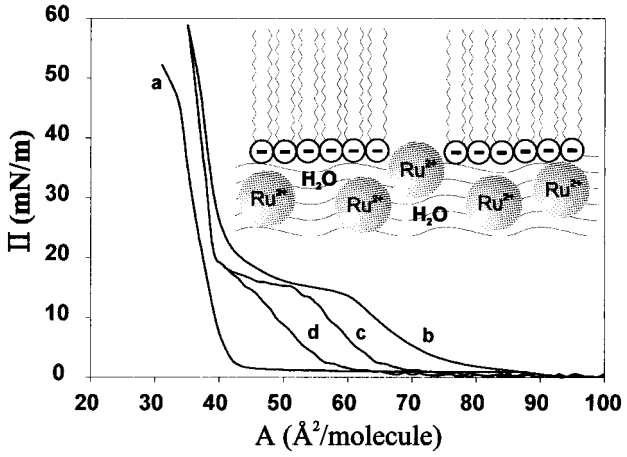

Figure 2. Surface pressure (Π) vs surface area (*A*) isotherms of DHP monolayers floating on pure water (pH 5.6, 21 ± 2 °C) (a) and on 1.0 × 10^{-4} M aqueous $Ru(bpy)_3Cl_2$ solution, initially compressed from Π = 0 to Π = 59 mN/m (b) and then expanded (c). The isotherm (d) was recorded after fifteen cycles of compression−decompression. All the compression and decompression cycles were performed at a barrier moving speed of 5 $Å^2$ mol^{-1} min^{-1}. The inset shows schematically the arrangements of the cationic ruthenium complexes as counterions at the DHP interface.

Transfer of Additional DHP/$[Ru(bpy)_3]^{2+}$ Layers onto Solid Substrates. Additional layers of DHP/$[Ru(bpy)_3]^{2+}$ were transferred by Schaefer's method.[22] This involved the placing of the inverted substrate (carrying DHP monolayer coated ruthenium complex crystallites, prepared as described above) horizontally above a compressed DHP monolayer floating above the aqueous $[Ru(bpy)_3]^{2+}$ complex subphase such that the hydrocarbon tails opposed each other (C in Figure 1). Using a mechanical device, the substrate was lowered until it barely touched the surface, and then it was carefully lifted at a low angle (ca. 10−20°) while maintaining a constant surface pressure at Π = 30 mN/m. During the lifting a meniscus formed and an overturned DHP monolayer was "sucked in". Thus using the Schaefer's method in the first instance resulted in the transfer of a bilayer with some $[Ru(bpy)_3]^{2+}$ complex crystallites sandwiched between the DHP headgroups and in the overall deposition of three DHP monolayers and two layers of $[Ru(bpy)_3]^{2+}$ crystallites onto the substrate (D in Figure 1). We shall refer to this structure as three layers of $[Ru(bpy)_3]^{2+}$/DHP film. Repeating this horizontal deposition onto the three layers of $[Ru(bpy)_3]^{2+}$/DHP film one, two, three, and four times led to the formation of five, seven, nine, and eleven layers of $[Ru(bpy)_3]^{2+}$/DHP films. After each Schaefer's transfer the excess material floating around the substrate edges was carefully wiped off by a tissue paper. Good transfer ratios (1.00 ± 0.05) were observed on using Schaefer's method for the deposition of multilayer $[Ru(bpy)_3]^{2+}$/DHP films onto solid substrates.

Absorption and Emission Spectroscopy. Bulk absorption and fluorescence spectra of aqueous $[Ru(bpy)_3][Cl_2]$ solutions and of single and multilayer $[Ru(bpy)_3]^{2+}$/DHP films were recorded on a diode array absorption spectrophotometer (Hewlett-Packard, 8452A) and on a SPEX fluorimeter combined with a rapid scan multichannel spectrometer (Tracor Northern, TN-6500), respectively.

Near-Field Scanning Optical Microscopy. A modified Topometrix Aurora near-field scanning optical microscope (NSOM) was employed to record all the topographic and near-field fluorescence images. The microscope stage was placed on a vibration-free optical table (Newport Inc.) where the measurements were conducted at room temperature under

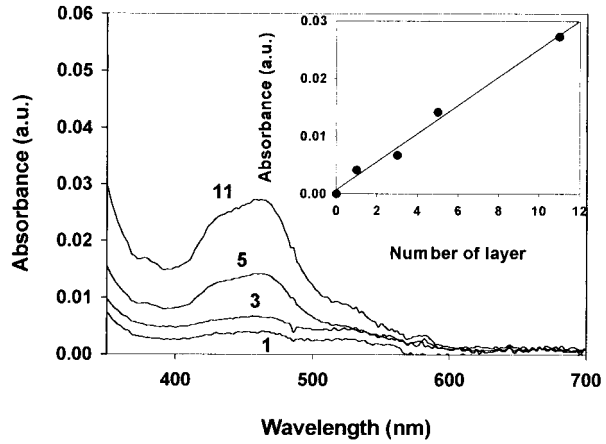

Figure 3. Absorption spectra of 1, 3, 5, and 11 layers of DHP/$[Ru(bpy)_3]^{2+}$ films transferred by horizontal lifting (1 layer) and by applying Schaefer's method repeatedly (3, 5, and 11 layers) onto a quartz substrate while maintaining a constant surface pressure of $\Pi = 30$ mN/m (see Experimental Section for details). Linearity of the absorbance peaks at 454 nm with the number of layers deposited is shown in the inset.

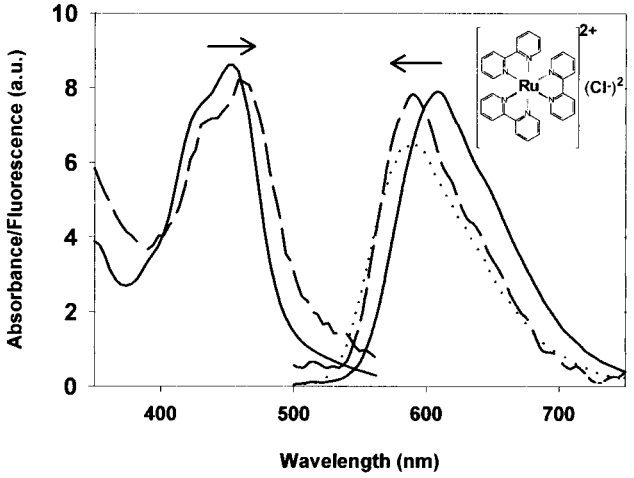

Figure 4. Absorption and fluorescence emission spectra of a 1.0×10^{-4} M aqueous $[Ru(bpy)_3][Cl_2]$ solution (solid lines) and those of 11 sandwich layers of DHP/$[Ru(bpy)_3]^{2+}$ film (broken lines). Also shown is the NSOM-imaged emission spectrum of a DHP monolayer supported $[Ru(bpy)_3]^{2+}$ crystallites, excited at 488 nm (dotted lines). The arrows above the spectra indicate the direction of the absorption and emission spectral shift on going from an aqueous $[Ru(bpy)_3][Cl_2]$ solution to the 11 sandwich layers of the DHP/$[Ru(bpy)_3]^{2+}$ film.

ambient conditions. Aluminum-coated optical fibers, tapered at the apex to form a 50−100 nm diameter aperture, were used as the illumination probe. A 488 nm light beam (0.5−1.0 mW) from a CW argon ion laser (Spectra Physics 2000) was coupled into the probe, delivering ca. 10^7 photons s^{-1} from the aperture. A piezoelectrically controlled sample stage provided sample motion in the *X*, *Y*, and *Z* (normal to the sample plane) directions. The sample was brought to the aperture and was held within the near field (5−10 nm) of the probe by an optical shear-force feedback mechanism which was accomplished optically with light from a 980 nm diode laser (EG&G Canada) focused onto the tip excited at its fundamental resonant frequency (70−80 kHz), reflected off the surface, and detected by a quarter split photodiode. Two retardation plates $\lambda/2$ and $\lambda/4$ (Melles Griot) were placed between laser outlet and fiber coupler to control the polarization of the incident light out of the probe aperture. Excitation of the sample via the tip generated photoluminescence, which was collected in the transmission mode by a 100×, 1.25 NA oil immersion objective (Zeiss) and filtered by two short-pass filters (CVI SPF-900) to remove residual 980 nm light and one band-pass filter (peak = 550 nm, bandwidth = 25 nm) to remove the 488 nm excitation light. The filtered light from the sample was then focused and imaged onto a single-photon-counting silicon avalanche photodiode detector (SAPD SPCM-200, EG&G, Canada). Images were acquired on at least three different areas of each sample at a scanning rate of 5 μm s^{-1}. For near-field fluorescence spectroscopy, the path of the transmitted light was directed through a compact monochromator (ISA, H10, 1200 g/mm).[13−15,18,19]

Results and Discussion

Monolayer Surface Pressure (Π) vs Surface Area (*A*) Isotherms. Surface pressure (Π) vs surface area (*A*) isotherms of DHP monolayers on pure water and on a 1.0×10^{-4} M aqueous solution of $[Ru(bpy)_3][Cl_2]$ are shown in Figure 2. Upon lateral compression, the DHP monolayer on pure water underwent a gaseous to liquid expanded (LE) phase transition in the pressure region between 2 and 5 mN/m and transferred promptly into a solid condensed (SC) phase (see curve a in Figure 2). The limiting headgroup area of a DHP molecule on H_2O was estimated to be 41 ± 1 Å^2 by extrapolating the Π−*A* isotherm to zero surface pressure. This value is in good agreement with previously published results (40.5,[12] 40,[23] and 41.5 Å^2/molecule[24]) and with that derived from space-filling (Corey-Pauling-Koltun (CPK)) models in which the long hydrocarbon chains are well packed in a 2D lattice (41 ± 1 Å^2/molecule).[25]

Π−*A* isotherms for DHP floating on a 1.0×10^{-4} M aqueous solution of $[Ru(bpy)_3][Cl_2]$ were found to be different from that observed on a pure water. Repeated compression and expansion cycles of the DHP monolayer on the $[Ru(bpy)_3]^{2+}$-containing subphase are shown in curves b, c, and d in Figure 2. The first compression manifested itself in the appearance of a liquid condensed (LC) state beginning at about 15 mN/m and prevailing between 63 and 42 Å^2, after which it transformed into the SC phase (see curve b in Figure 2). On a consecutive expansion and compression the Π−*A* isotherms shifted toward smaller area, suggesting the irreversible formation of an SC phase (see curve c in Figure 2). Similar large hysteresis and significant phase changes for a DHP monolayer floating on aqueous tetraazophthalocyanines or tetrapyridylporphyrins have been reported.[25]

Consecutive compressions and expansions of the DHP monolayer on a 1.0×10^{-4} M aqueous solution of $[Ru(bpy)_3][Cl_2]$ resulted in progressive shifts of the Π−*A* isotherms toward smaller area, with a liquid-phase onset at 74 Å^2/molecule and LC coexistence phase onset at 45 Å^2/molecule, respectively. After 15 compression and expansion cycles, the compression Π−*A* isotherm showed a liquid-phase onset converging to 44 Å^2/molecule, a value close to the DHP molecular area, and no observable LC phase (see curve d in Figure 2). These observations imply that the SC phase grows at the expense of the LC counterparts by means of dynamic intralayer interactions mediated by the repeated compression−expansion cycles. Similar hysteresis of the Π−*A* isotherms for DHP monolayers floating on aqueous NaCl solution was rationalized in terms of changes in hydration and adhesion forces originating in charge neutralization and/or counterion shielding of the phosphate headgroups in DHP.[24] It is likely, therefore, that repulsive interactions between the phosphate headgroups in DHP monolayers are reduced by the surrounding $[Ru(bpy)_3]^{2+}$ ions.[26]

Charged DHP molecules in the monolayer interact repulsively with each other to form preferentially a loosely packed phase,

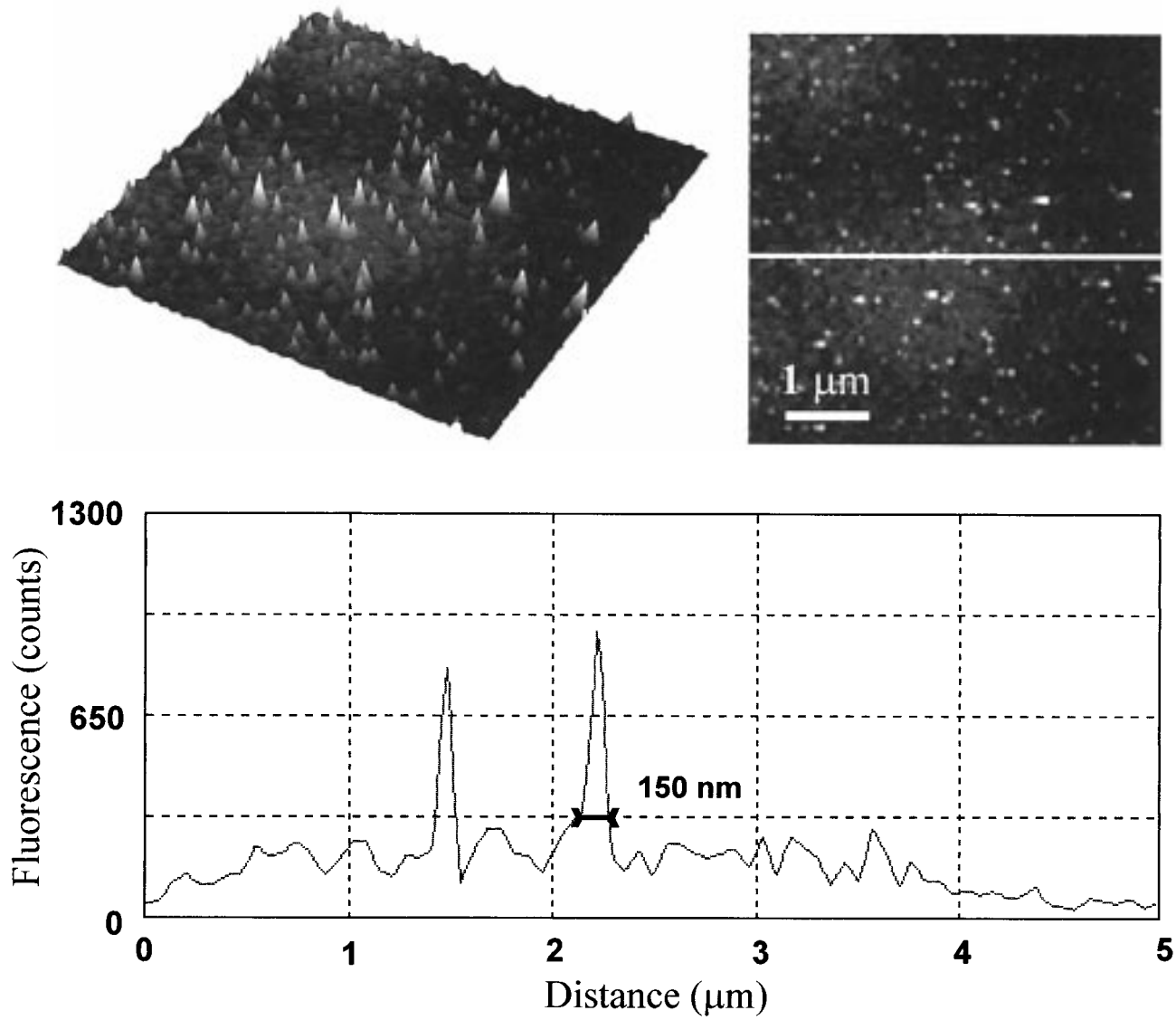

Figure 5. Near-field fluorescence image of DHP monolayer supported $[Ru(bpy)_3]^{2+}$ crystallites, transferred at $\Pi = 16$ mN/m. The bright spots in the 5 μm by 5 μm (300 by 300 pixels, 10 ms per pixel) image result from emission from clustered $[Ru(bpy)_3]^{2+}$ molecules. The fwhh of the subdiffraction-limited spots is shown to be 150 nm on the line scan profile.

similar to the LE phase even at high surface pressure (e.g., 30 mN/m). This intralayer repulsion is defined, in terms of the electrostatic contribution to the surface pressure, on the 2D charge density by[24]

$$\Pi_{EL} = \frac{\sqrt{S^2+1}-1}{eS} 2kT\sigma \qquad (1)$$

where k is the Boltzmann constant, T is the absolute temperature, e is the charge of the proton, σ is the surface charge density, and S is a dimensionless parameter defined by

$$S = \frac{\sigma}{\sqrt{8kTn\epsilon_r\epsilon_0}} \qquad (2)$$

where n is the number density of ions in the bulk solution, ϵ_r is the relative dielectric constant of water, and ϵ_o is the dielectric permittivity of vacuum.

As a requirement of using this equation, we have to assume that the variation of the surface pressure is caused by electrostatic interactions only,[24] and then we can estimate the charge density of the DHP monolayer floating on an aqueous $[Ru(bpy)_3]^{2+}$ solution. At $A = 80$ Å^2/molecule (Figure 2), the surface pressures for the DHP monolayer on pure water and on aqueous $[Ru(bpy)_3]^{2+}$ are respectively $\Pi = 1.8$ mN/m and $\Pi = 2.2$ mN/m. The charge density for the DHP monolayer on the metal complex subphase is then calculated by the eq 1 to be 12 nm^2 per charge (that is, there is one charge for every 15 DHP molecules). For the DHP monolayer on the aqueous NaCl subphase, the two-dimensional charge density was estimated to be in the range 15−25 nm^2 per charge at pH = 5.5.[24] However, it should be noted that the counterion effect of NaCl is to reduce the charge density by neutralizing the deprotonated phosphates, while that of the divalent $[Ru(bpy)_3]^{2+}$ species is expected to increase the charge density. Binding of counterionic species at the air/water interface neutralizes the surface charge and, in turn, reduces the intralayer force, leading to a more condensed state at a given surface pressure. These facts indicate that the charge density is large and is dominated by the neutralization of the DHP by $[Ru(bpy)_3]^{2+}$ species in the subphase.[24] From these results we can deduce that the $[Ru(bpy)_3]^{2+}$ ion, being appreciably hydrophilic, is forced to stay in the vicinity of the phosphoric acid moiety of the DHP monolayer.

Optical Spectroscopy of LB Films on Solid Substrates. A convenient way to monitor the successive depositions of DHP/$[Ru(bpy)_3]^{2+}$ layers onto substrates is to determine the increase of the absorbance of the 460 nm peak, due to the $[Ru(bpy)_3]^{2+}$ MLCT transition (Figure 3). The inset in Figure 3 displaying the observed linear relationship between the peak absorbance at 460 nm and the number of layers deposited substantiated the regularity of the ultrathin films produced. The two-dimensional number density of $[Ru(bpy)_3]^{2+}$ molecules in the films was calculated to be 0.65 molecule/nm^2 by using a molar extinction coefficient[27] of $\epsilon_{452-nm} = 14\,300\ M^{-1}\ cm^{-1}$ and the observed absorbance (Figure 3). This value is in good agreement with the expected stoichiometry of $[Ru(bpy)_3]^{2+}$:DHP = 1:2.

The optical properties of $[Ru(bpy)_3]^{2+}$ in the DHP films are compared to those in aqueous solutions in Figure 4. Absorption spectra of $[Ru(bpy)_3]^{2+}$ in these two media are characterized by peaks at 460 and 454 nm and shoulders at 440 and 435 nm, respectively (Figure 4). The 6 nm red shift of the absorption in the DHP film with respect to that in aqueous solution (indicated by the arrow above the absorption bands) is the consequence of the change in the microenvironment of $[Ru(bpy)_3]^{2+}$ in these two media. The emission maxima of $[Ru(bpy)_3]^{2+}$ in an aqueous solution and in the DHP films are governed by the charge transfer between the d-ground-state orbital of the metal ion and the π^*-antibonding orbital on the ligand (metal ligand charge transfer)[28] at 609 and 589 nm (Figure 4). This blue shift of the emission maxima (indicated by the arrow above the emission bands) suggests a hydrophilic and rigid nature of the microenvironment in the DHP film and a strong interaction between the dialkyl phosphate headgroup and the metal complex ion.[10]

Near-Field Scanning Optical Microscopy of $[Ru(bpy)_3]^{2+}$ Supported by DHP Monolayers. Submicron morphologies of DHP monolayer supported $[Ru(bpy)_3]^{2+}$ crystallites, transferred onto solid glass substrates at different surface pressures, were spatially and spectrally resolved by near-field scanning optical microscopy.

A typical fluorescence image of $[Ru(bpy)_3]^{2+}$ crystallites, transferred at $\Pi = 16$ mN/m (LE phase), is seen to consist of bright spots (Figure 5). Since these spots persistently appeared in the images of a repeatedly scanned area, they were attributed to the fluorescence of clusters composed of a few hundred $[Ru(bpy)_3]^{2+}$ molecules.[14] The clusters seemed to be thinly spread. Indeed, only two fluorescent peaks were found in the 5 μm line scan shown (Figure 5). The peaks exhibited a full width at half-maximum (fwhm) of ca. 100−200 nm, and their average intensity was found to be 1000 photons s^{-1} (with 10^7 photons s^{-1} excitation) on a dark background of less than 10 photons s^{-1}.

As the DHP monolayer was compressed into the LE/LC coexistence region, circular domains containing $[Ru(bpy)_3]^{2+}$ species became dominant (Figure 6A). Repeated compression and expansion of the DHP monolayer, supporting the $[Ru(bpy)_3]^{2+}$ crystallites, markedly affected the fluorescence images. This is illustrated by the NSOM image (Figure 6B), taken after two compression and expansion cycles of the DHP monolayer supported $[Ru(bpy)_3]^{2+}$ crystallites. The colonies, consisting of interconnected bright spots, with dimension of ca. 2−3 μm in diameter surrounded by a dark background shown in Figure 6B are believed to correspond to $[Ru(bpy)_3]^{2+}$ clusters attached at disconnected DHP condensed domains. The topography of the same sample (not shown) indicated heights at the center of these colonies (ca. 70 nm) which were twice as high as those observed for the films deposited from monolayers in their LE phase.

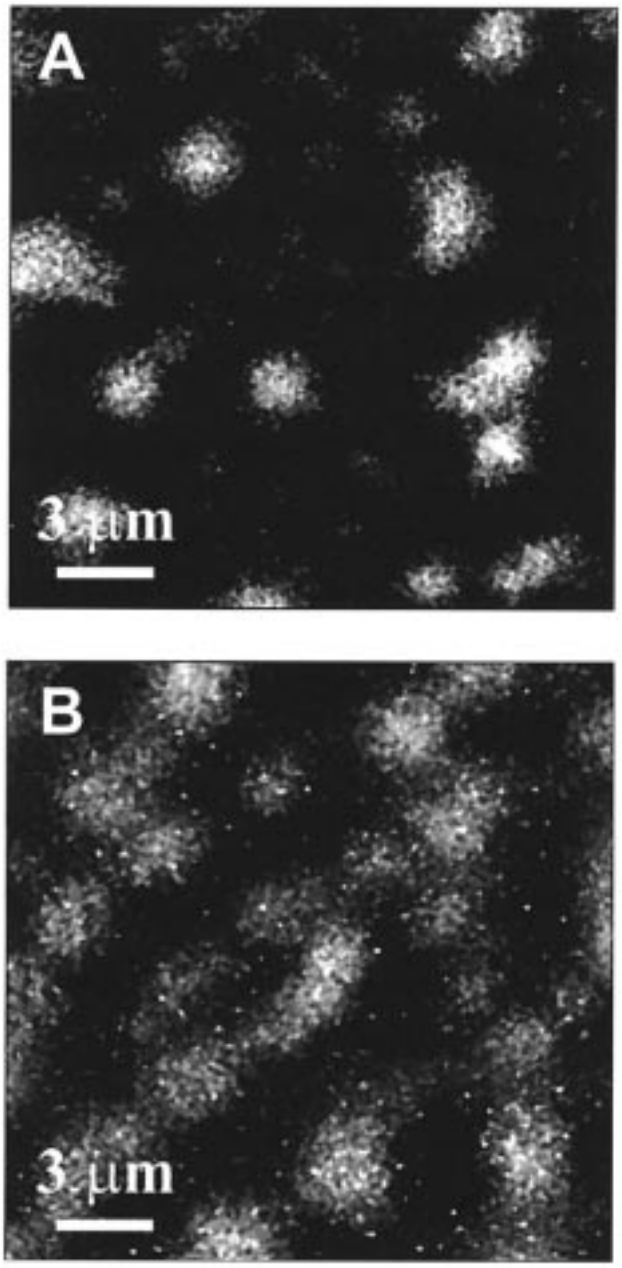

Figure 6. Near-field fluorescence images of DHP monolayer supported $[Ru(bpy)_3]^{2+}$ clusters deposited at $\Pi = 30$ mN/m during the first compression (A) and after two cycles of compression−decompression (B). A change in the concentration of the fluorescing species in the circular domains is seen to accompany the compression and expansion of the DHP monolayer.

Formation of the fluorescent colonies can be accounted for by the presence of locally concentrated $[Ru(bpy)_3]^{2+}$ species which accumulated under the DHP monolayer prior to their transfer to the substrate. Alternatively, clusters may be formed within the headgroups of the DHP layer through lateral migration of the adsorbed $[Ru(bpy)_3]^{2+}$ molecules after deposition. In the latter case, the DHP film provides a two-dimensional template which limits the cluster growth. The present data are insufficient to distinguish between these possibilities; indeed alternative mechanisms for cluster formation cannot be excluded.

Further consecutive compression and expansion cycles of the DHP monolayer floating on $[Ru(bpy)_3]^{2+}$ resulted in the transformation of circular colonies to needle-like structures. This is illustrated by the near-field fluorescence images taken after seven and fifteen compression and expansion cycles (Figures 7

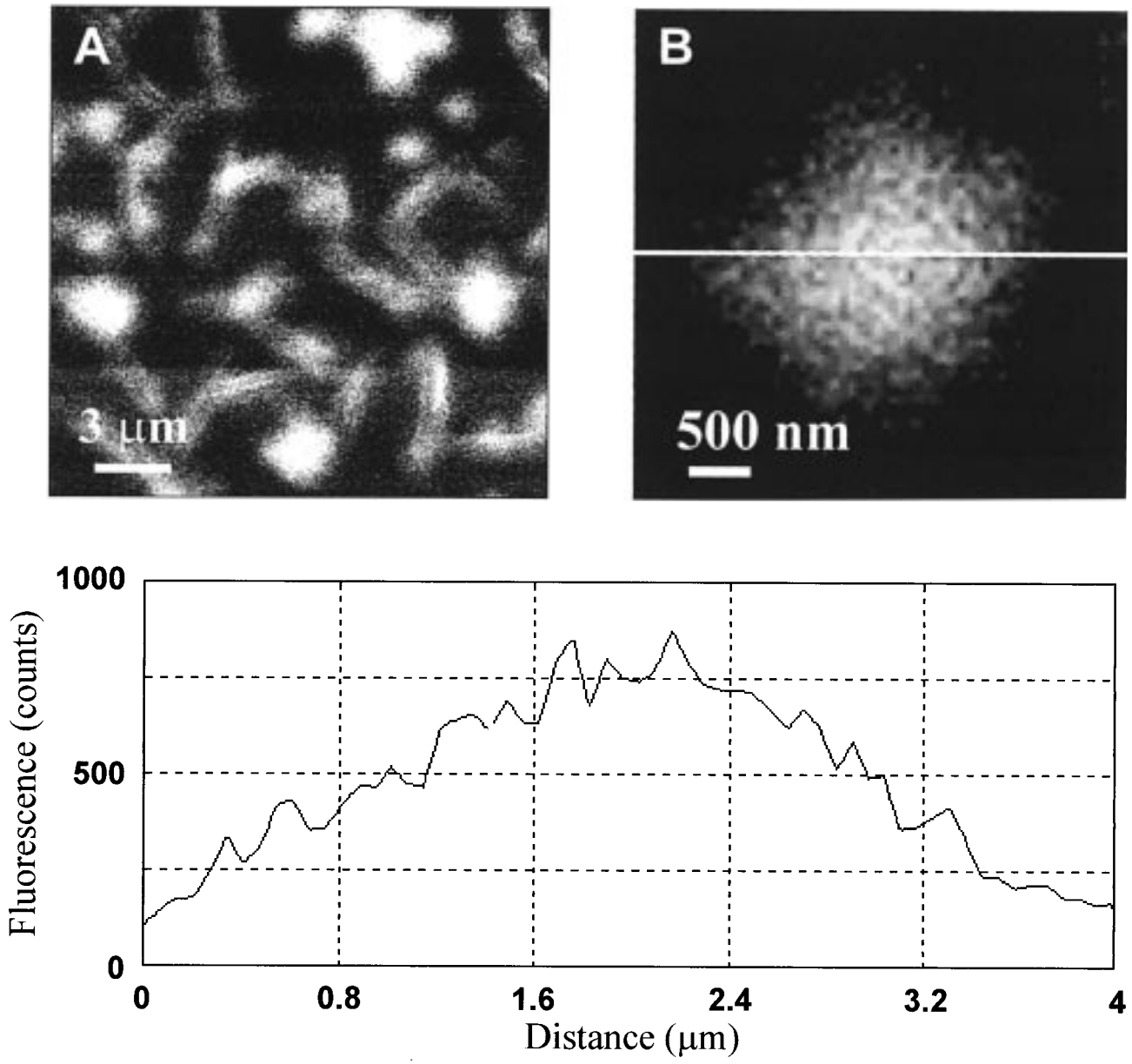

Figure 7. Coexistence of $[Ru(bpy)_3]^{2+}$ clusters, microcrystallites, and circle-shaped domains after seven cycles of compression−decompression treatment (A) and the spatially resolved fine structure of one single circle-shaped domain by near-field fluorescence imaging at 590 nm (B). The DHP monolayer, along with the $[Ru(bpy)_3]^{2+}$ crystallites grown under it, was deposited at $\Pi = 18$ mN/m. A line scan profile also provides information on the circular domain boundaries of the fluorescent $[Ru(bpy)_3]^{2+}$ species.

and 8). In the NSOM image, taken after seven consecutive compression and expansion cycles, the fluorescence intensities at the centers of the colonies (ca. 800 photons s^{-1}) were found to be considerably higher than those located in the "needles" (ca. 500 photons s^{-1}), although the geometrical heights of the former were observed to be smaller than the latter (Figure 7A). Figure 7B and its line scan profile shows that the fluorescence gradually diminishes across the LE/LC domain boundary, rather than exhibiting the sharp discontinuity of a simple phase boundary. Further growth of the crystals was observed after performing additional compression and expansion cycles of the DHP monolayer floating on $[Ru(bpy)_3]^{2+}$ crystallites.

NSOM topographic and corresponding near-field fluorescence images of $[Ru(bpy)_3]^{2+}$ microcrystallites harvested after fifteen compression and expansion cycles of the supporting DHP monolayer are shown in Figure 8. The length of these "needles" was found to range from 1.5 to 5.5 μm, and their heights were less than 300 nm (vide supra). The lateral mobility of the adsorbed $[Ru(bpy)_3]^{2+}$combined with the forced interconnection caused by the compression expansion cycles facilitated the growth of these needlelike crystallites. Similar behavior has been observed in the mechanically induced crystallization of cyanine-dye J-aggregates under monolayers upon repeated compression and expansion cycles.[4,25]

A number of needlelike $[Ru(bpy)_3]^{2+}$ crystallites appears to be twinned (see the topographic and fluorescence NSOM images in Figure 8). The pairing of the crystallites is likely to be favored by the repulsive dipolar interaction of the $[Ru(bpy)_3]^{2+}$ molecules within a domain and aided by mechanical manipulation which brings separately developed crystals together in preferred orientation. The bright circular domains observed on the NSOM fluorescence images (Figure 8B,D,F) are not present on the corresponding topographic images (Figure 8A,C,F), suggesting that after several compression and expansion cycles the circular domains disappear at the expense of the less fluorescent bigger crystals. These results allow a useful comparison of the

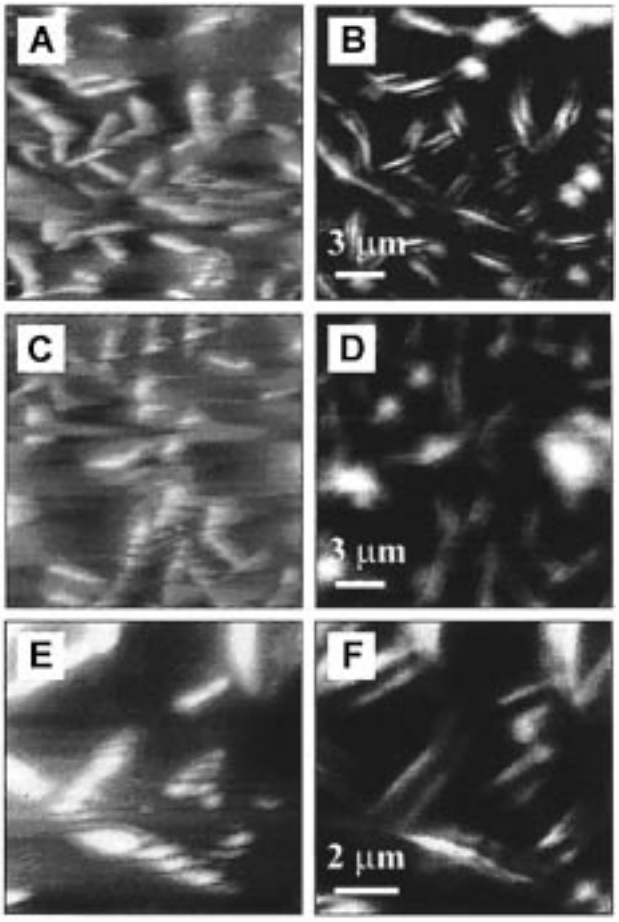

Figure 8. NSOM topographic (A, C, and E) and corresponding near-field fluorescence (B, D, and F) images of DHP monolayer-attached $[Ru(bpy)_3]^{2+}$ crystallites transferred onto a glass substrate at $\Pi = 18$ mN/m after 15 consecutive compression and expansion cycles of the monolayer. The bright circular domains observed on the NSOM fluorescence images are not present on the corresponding topographic images.

topographic and spatially resolved emission images and substantiate the power of NSOM to reveal subtle structural information.

In-site near-field optical spectroscopy yielded also information on the electronic properties of single $[Ru(bpy)_3]^{2+}$ entities. Nanoscopic scale near-field optical excitation into the electronic absorption of the metal-to-ligand charge-transfer transition of Ru(II) leads to the observation of site-resolved fluorescence emission (see dotted line spectrum in Figure 4). After obtaining the NSOM fluorescence image of the sample, the tip was positioned above a chosen spot (either a circular domain or a single needlelike microcrystal). The tip was then placed in close proximity to the sample using the shear-force feedback system. The spectrum acquisition time was no more than 30 s. The circular domains gave a spectrum (not shown) matching that obtained for an aqueous $[Ru(bpy)_3][Cl_2]$ (i.e., belonging to well-dispersed molecules). Conversely the emission spectrum of the needlelike microcrystallites showed features typical for aggregated $[Ru(bpy)_3]^{2+}$ crystallites (see broken and dotted lines in Figure 4).

Conclusion

Surface charges and charge densities govern the observed microcrystallization of cationic ruthenium complexes under monolayers. The phosphate headgroup of DHP possesses an active hydrogen which can be exchanged by a positively charged $[Ru(bpy)_3]^{2+}$ species in basic solutions. Such Coulombic attractions are responsible for the high $[Ru(bpy)_3]^{2+}$ ion concentration at the monolayer interface. NSOM has been demonstrated to be an eminently suitable method for observing the initial stages of microcrystallization under monolayers. This method, which offers all the advantages of optical microscopy plus the high resolution of scanning probe microscopy, has permitted the observation of features within a single domain with submicron resolving power (<50 nm). Fluorescence imaging has been shown to offer better spatial resolution than shear-force imaging by using the same probe.

The initially observed circular spots, obtained during first compression of freshly spread monolayer (Figure 6A,B), are not attributable to single $[Ru(bpy)_3]^{2+}$ molecules but to small clusters of them which serve as "seeds" for crystal growth. Apparently, the compression−expansion cycles increased the contact between the seeds themselves and/or with larger clusters of crystals. This manifested itself in the development of more intense and differently shaped $[Ru(bpy)_3]^{2+}$ crystallites (Figure 7).

Acknowledgment. Support of this work by the New York State Science and Technology Foundation and Clarkson University's Center for Advanced Materials Processing (CAMP) is gratefully acknowledged.

References and Notes

(1) Fendler, J. H. *Membrane-Mimetic Approach to Advanced Materials*; Springer-Verlag: Heidelberg, 1994.
(2) Weissbuch, I.; Popovitz-Biro, R.; Lahav, M.; Leiserowitz, L. *Acta Crystallogr.* **1995**, *B51*, 115−148.
(3) Weissbuch, I.; Guo, S.; Edgar, R.; Cohen, S.; Howes, P.; Kjaer, K.; Als-Nielsen, J.; Lahav, M.; Leiserowitz, L. *Adv. Mater.* **1998**, *10*, 117−121.
(4) Kirstein, S.; Möhwald, H. *Chem. Phys. Lett.* **1989**, *154*, 303−308.
(5) Schmitt, F. J.; Meller, P.; Ringsdorf, H.; Knoll, W. *Prog. Colloid Polym. Sci.* **1990**, *83*, 136−145.
(6) Kirstein, S.; Möhwald, H. *Adv. Mater.* **1995**, *7*, 460−463.
(7) Kirstein, S.; Steitz, R.; Garbella, R.; Möhwald, H. *J. Chem. Phys.* **1995**, *103*, 818−825.
(8) Kirstein, S.; Möhwald, H. *J. Chem. Phys.* **1995**, *103*, 826−833.
(9) Samha, H.; DeArmond, M. K. *Langmuir* **1994**, *10*, 4157−4163.
(10) Murakata, T.; Miyashita, T.; Matsuda, M. *J. Phys. Chem.* **1988**, *92*, 6040−6043.
(11) Frostman, L. M.; Ward, M. D. *Langmuir* **1997**, *13*, 330−337.
(12) Bettarini, S.; Bonosi, F.; Gabrielli, G.; Martini, G.; Puggelli, M. *Thin Solid Films* **1992**, *210*, 42−45.
(13) Betzig, E.; Trautman, J. K. *Science China* **1992**, *257*, 189−195.
(14) Xie, X. S.; Dunn, R. C. *Science* **1994**, *265*, 361−364.
(15) Paesler, M. A.; Moyer, P. J. *Near-field Optics−Theory, Instrumentation and Applications*; Wiley-Interscience: New York, 1996.
(16) Kirsch, A. K.; Schaper, A.; Huesman, H.; Rampi, M. A.; Mobius, D.; Jovin, T. M. *Langmuir* **1998**, *14*, 3895−3900.
(17) Shiku, H.; Dunn, R. C. *J. Phys. Chem. B* **1998**, *102*, 3791−3797.
(18) Vanden Bout, D. A.; Kerimo, J.; Higgins, D. A.; Barbara, P. F. *Acc. Chem. Res.* **1997**, *30*, 204−212.
(19) Higgins, D. A.; Barbara, P. F. *J. Phys. Chem.* **1995**, *99*, 3−7.
(20) Tamm, L. K.; Böhm, C.; Yang, J.; Shao, Z.; Hwang, J.; Edidin, M.; Betzig, E. *Thin Solid Films* **1996**, *284*, 813−816.
(21) Hwang, J.; Tamm, L. K.; Böhm, C.; Ramalingam, T. S.; Betzig, E.; Edidin, M. *Science* **1995**, *270*, 610−614.
(22) Langmuir, I.; Schaefer, V. J. *J. Am. Chem. Soc.* **1938**, *57*, 1007.
(23) Caminati, G.; Gabrielli, G.; Barni, E.; Savarino, P.; Möbius, D. *Prog. Colloid Polym. Sci.* **1992**, *89*, 223−226.
(24) Claesson, P.; Carmona-Ribeiro, A. M.; Kurihara, K. *J. Phys. Chem.* **1989**, *93*, 917−9.
(25) Gregory, B. W.; Vaknin, D.; Gray, J. D.; Ocko, B. M.; Stroeve, P.; Cotton, T. M.; Struve, W. S. *J. Phys. Chem. B* **1997**, *101*, 2006−2019.
(26) Lefevre, D.; Porteu, F.; Balog, P.; Roulliay, M.; Zalczer, G.; Palacin, S. *Langmuir* **1993**, *9*, 150.
(27) Kalyanasundaram, K.; Kiwi, J.; Gratzel, M. *Helv. Chim. Acta* **1978**, *61*, 2720.
(28) Kalyanasundaram, K. *Coord. Chem. Rev.* **1982**, *46*, 159−244.